






# Strong covalent interaction Fe<sub>2</sub>O<sub>3</sub>/nitrogen-doped porous carbon fiber hybrids as free-standing anodes for lithium-ion batteries

Weiyang Li<sup>1</sup> , Fan Yang<sup>1</sup> , Yichuan Rui<sup>1,\*</sup> , and Bohejin Tang<sup>1,\*</sup> 

<sup>1</sup> College of Chemistry and Chemical Engineering, Shanghai University of Engineering Science, Shanghai 201620, China

Received: 22 October 2018

Accepted: 3 January 2019

Published online:  
11 January 2019

© Springer Science+Business  
Media, LLC, part of Springer  
Nature 2019

## ABSTRACT

A simple and novel method that combines the electrospinning technology with nonaqueous sol–gel method is developed to incorporate Fe<sub>2</sub>O<sub>3</sub> nanoparticles into ZIF-8-derived nitrogen-doped highly porous carbon fibers (NPCFs). The size of Fe<sub>2</sub>O<sub>3</sub> nanoparticles is about 5 nm. The interfacial interaction between Fe<sub>2</sub>O<sub>3</sub> and NPCFs is investigated by thermogravimetric analysis, Raman spectrum and X-ray photoelectron energy spectrum. We found that Fe<sub>2</sub>O<sub>3</sub> nanoparticles are anchored strongly in the NPCFs through the Fe–O–C covalent bond. The impact of the Fe<sub>2</sub>O<sub>3</sub> content in the composites on electrochemical performance is also studied. When served as the flexible and free-standing anode of lithium-ion batteries (LIBs), the Fe<sub>2</sub>O<sub>3</sub>/NPCFs-66.9% exhibits superior electrochemical performance with the high discharge capacity of 1351 mA h g<sup>-1</sup> at 50 mA g<sup>-1</sup>, remarkable rate capability (337 mA h g<sup>-1</sup> even at 5000 mA g<sup>-1</sup>), and stable cycling performance (1106 mA h g<sup>-1</sup> after 100 cycles at 100 mA g<sup>-1</sup>). The excellent anodic property can be ascribed to the ultra-small size of Fe<sub>2</sub>O<sub>3</sub> nanoparticles, and the one-dimensional (1D) structure combined with the excellent electrical conductivity of NPCFs matrix. Moreover, the robust interfacial interaction Fe–O–C bond can restrain the aggregation of Fe<sub>2</sub>O<sub>3</sub> nanoparticles and accommodate the volume change. This can effectively maintain the integrity of the whole electrode during the long-term cycles. The results show that the composite may be considered as a promising anode material for advanced LIBs.

## Introduction

Lithium-ion batteries (LIBs) as the most popular energy storage device have attracted widespread attentions because of their high storage capacities, stable cycling and high safety [1–3]. However, the

low theoretical capacity of conventional graphite anode material (372 mA h g<sup>-1</sup>) has inhibited the further application for next-generation high-energy LIBs. Iron oxides, such as Fe<sub>2</sub>O<sub>3</sub> and Fe<sub>3</sub>O<sub>4</sub>, are attractive anode materials for LIBs due to their natural abundance, eco-friendly and low cost. In

Address correspondence to E-mail: ryc713@126.com; tangbohejin@sues.edu.cn

addition, the theoretical capacities of  $\text{Fe}_2\text{O}_3$  and  $\text{Fe}_3\text{O}_4$  are as high as 1007 and 926  $\text{mA h g}^{-1}$ , respectively ( $\text{Fe}_2\text{O}_3 + 6\text{Li} \leftrightarrow 3\text{Li}_2\text{O} + 2\text{Fe}$  and  $\text{Fe}_3\text{O}_4 + 8\text{Li} \leftrightarrow 4\text{Li}_2\text{O} + 3\text{Fe}$ ) [4–6]. However, iron oxides exhibit rapid capacity degradation and inferior cycling stability because of the low intrinsic electrical conductivity (below  $10^{-6} \Omega^{-1} \text{cm}^{-1}$ ) [7], the formation of unstable SEI film and the electrode collapse caused by the large volume expansion during the charge/discharge process (over 200%) [8]. Generally, two effective methods have been employed to surmount the above issues. One is to minimize the particles size down to the nanoscale. Taroscon's group has reported that nano-sized  $\text{Fe}_2\text{O}_3$  electrode exhibits the significant improvement in electrochemical performance compared with micro-sized  $\text{Fe}_2\text{O}_3$  electrode [9, 10]. The nano-sized particles can shorten the diffusion path of Li ions and minimize the strain to alleviate the absolute volume expansion. Another strategy is to incorporate carbon materials to form  $\text{Fe}_2\text{O}_3$ /carbon composites, which has been considered as the most effective method to overcome the above issues. Carbon materials including carbon nanotubes [11], carbon aerogel [12], carbon nanofiber [13], grapheme [14] and N-doped graphene aerogel [15] can not only release the residual stress arising from volume expansion of  $\text{Fe}_2\text{O}_3$  particles, but also enhance the electrical conductivity and restrain the particle agglomeration. Xiao et al. [16] reported a facile hydrothermal method to prepare  $\text{Fe}_2\text{O}_3$ /graphene composite, which showed a high reversible capacity up to 1069  $\text{mA h g}^{-1}$  at a current density of 50  $\text{mA g}^{-1}$  after 50 cycles. Nevertheless, the irreversible aggregation and restacking caused by the strong  $\pi$ - $\pi$  stacking and van der Waals force can easily occur and severely affect the electrochemical performance [17]. Wang et al. developed a one-pot solvothermal method to fabricate carbon coated  $\text{Fe}_2\text{O}_3$  composites [18]. However, the thin carbon film with a thickness of about 6 nm leads to a reduction of the contact interface between  $\text{Fe}_2\text{O}_3$  and the electrolyte and the core-shell structure does not have appropriate void space to accommodate the volume expansion of  $\text{Fe}_2\text{O}_3$  particles during cycling [19, 20]. Therefore, the challenge in obtaining reasonable structure and high-performance  $\text{Fe}_2\text{O}_3$ /carbon anode materials for LIBs still remains.

Metal organic frameworks (MOFs) as emerging porous material have received growing attentions because of their unique structure, tunable pore sizes,

and extensive applications in gas storage and separation, catalysts, drug delivery and so on [21]. In addition, the various pore size and large specific surface area of MOFs make them feasible as templates to prepare porous carbon materials, such as Ni-MOF, MOF-2, MOF-5, ZIF-8, etc. [22–26]. Furthermore, heteroatoms (e.g., B, S, N, and P) existed in the organic ligands of MOFs are vital to synthesize heteroatoms doping in the MOFs-derived carbonaceous materials [27]. Among them, N-doping in carbon materials is considered as the most effective approach to improve electronic conductivity of carbon materials by creating extrinsic defects [28]. ZIF-8 is the most popular precursors to prepare carbon materials because of the high content of N in 2-methylimidazolate ( $\approx 34 \text{ wt\%}$ ) [29]. However, only conventional assembly processes can be employed for most of those MOFs-derived powdery carbons materials. The polymer binder and conductive additives will increase the contact resistance and lower the rate capability due to their insulativity and electrochemical inactivity. Therefore, the design and fabrication of flexible and free-standing electrode materials have been considered as the trend of development in LIBs. In this regard, researchers have elaborately designed kinds of  $\text{Fe}_2\text{O}_3$ /carbon electrode materials that eradicate the usage of binder and current collectors in traditional battery electrode configuration, such as  $\text{Fe}_2\text{O}_3$ @ carbon/carbon cloth [18],  $\text{Fe}_2\text{O}_3$ /graphene/carbon nanotubes [30],  $\text{Fe}_2\text{O}_3$ /nanotubes [31], and  $\text{Fe}_2\text{O}_3$ /carbon nanofiber [19] and so on. But the usage of nano-sized MOFs-derived carbons as basic architectural units in 1D to construct flexible and free-standing  $\text{Fe}_2\text{O}_3$ /carbon electrode is rarely explored. As a convenient and inexpensive industry-viable technology, electrospinning has been widely employed to prepare 1D nanomaterials with controllable morphology and compositions [32].

In this paper, a novel strategy that combines the electrospinning technology with nonaqueous sol-gel method is developed to incorporate  $\text{Fe}_2\text{O}_3$  nanoparticles into ZIF-8-derived nitrogen-doped highly porous carbon fibers (NPCFs). Benefiting from the smaller size of  $\text{Fe}_2\text{O}_3$  nanoparticles (about 5 nm), robust 1D structure and superior electrical conductivity of NPCFs as well as the strong covalent bond interactions (Fe–O–C bond) between  $\text{Fe}_2\text{O}_3$  and NPCFs, the electrochemical performance of  $\text{Fe}_2\text{O}_3$  nanoparticles has been distinctively improved after incorporating it into NPCFs. We also explore the

effect of different loading densities on the electrochemical performance of the composites. The Fe<sub>2</sub>O<sub>3</sub>/NPCFs-66.9% exhibits the best rate (337 mA h g<sup>-1</sup> at 5000 mA g<sup>-1</sup>) and cycling performances (1106 mA h g<sup>-1</sup> after 100 cycles at 100 mA g<sup>-1</sup>). In addition, the preparation processes are convenient and time-saving, and the raw materials are natural abundance, eco-friendliness and low cost. Therefore, the flexible and free-standing Fe<sub>2</sub>O<sub>3</sub>/NPCFs-66.9% composite shows promising applications as anodes material for LIBs.

## Experimental section

### Synthesis of the ZIF-8 nanoparticles

All chemicals were purchased from Sigma-Aldrich and used without further purification. Zn(NO<sub>3</sub>)<sub>2</sub>·6H<sub>2</sub>O (0.3 g) was dissolved in methanol (20 mL) to form a solution. 2-methylimidazole (0.6 g) was dissolved in methanol (10 mL) to form another clear solution. Then, the two solutions were mixed together, and stirred for 2 h in an ice bath. After that, the white powers were washed with methanol for five times by centrifugation (10,000 rpm, 10 min) and dried at 90 °C under vacuum for 24 h.

### Synthesis of ZIF-8-derived nitrogen-doped porous carbon fibers (NPCFs)

In a typical synthesis, 0.8 g ZIF-8 power was mixed with 5 mL *N,N*-dimethylformamide (DMF) under ultrasonic until it was well dispersed. Then, 0.4 g polyacrylonitrile (PAN,  $M_w = 150,000$  g mol<sup>-1</sup>) was added into the above solution and stirred at 65 °C for 6 h to prepare the electrospinning precursor. The electrospinning process was executed at a high positive voltage 18 kV and the collect distance was 15 cm between the electrospinning jet and alumina foil collector. The flow rate was 0.5 mL h<sup>-1</sup>. The as-prepared fibers were peeled off from the alumina foil and then carbonized in a furnace at 800 °C for 2 h with a heating rate of 2 °C min<sup>-1</sup> in N<sub>2</sub> flow. The obtained sample was washed with dilute HCl and deionized water for several times to remove the remanent Zn component. The ZIF-8-derived NPCFs was finally synthesized.

### Synthesis of Fe<sub>2</sub>O<sub>3</sub> nanoparticles and Fe<sub>2</sub>O<sub>3</sub>/NPCFs composites

The Fe<sub>2</sub>O<sub>3</sub>-NPCFs hybrid was fabricated via a facile one-step nonaqueous sol-gel coassembly with controllable mass ratio that can be directly used as free-standing anodes. In briefly, 0.423 g ferric trichloride hexahydrate (FeCl<sub>3</sub>·6H<sub>2</sub>O) was dissolved in 10 mL tetrahydrofuran (THF) with the help of ultrasonication to get the Fe-based precursor solution. Then, 0.029 g of NPCFs was immersed into the above Fe-based precursor solution for 24 h at room temperature. Finally, the above mixed suspension was pyrolyzed in a flask at 250 °C and kept 2 h to convert the Fe-based precursor to Fe<sub>2</sub>O<sub>3</sub>. The Fe<sub>2</sub>O<sub>3</sub>/NPCFs mats were obtained by washing with THF five times and absolute ethanol five times, and drying at 90 °C for 20 h in vacuum. For comparison, the controllable mass ratio was prepared by the same process except changing the FeCl<sub>3</sub>·6H<sub>2</sub>O to 0.232 and 0.725 g, respectively. The as-synthesized composites were labeled as Fe<sub>2</sub>O<sub>3</sub>/NPCFs-66.9%, Fe<sub>2</sub>O<sub>3</sub>/NPCFs-41.1% and Fe<sub>2</sub>O<sub>3</sub>/NPCFs-79.2%, respectively. Fe<sub>2</sub>O<sub>3</sub> bulk counterpart was synthesized by the same process as the Fe<sub>2</sub>O<sub>3</sub>-NPCFs samples. The only difference was that NPCFs was not added in the above Fe-based precursor.

### Materials characterization

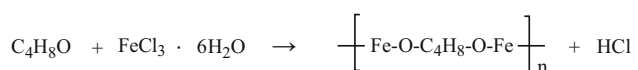
The crystalline structures of the as-synthesized products were examined by X-ray diffraction (XRD, Bruker D<sub>2</sub> Phaser X-ray Diffractometer, Cu K $\alpha$  radiation). X-ray photoelectron spectroscopy (XPS) experiments were carried out on Thermo ESCALAB 250XI using an Al K $\alpha$  X-ray source. Raman scattering spectra were recorded with a Renishaw System 2000 spectrometer. Thermogravimetry (TG) measurement was carried out on a TA Instruments Hi-Res TGA 2950 from 30 to 700 °C at a rate of 10 °C min<sup>-1</sup> in flowing air. Nitrogen adsorption/desorption measurements were carried out on a Micromeritics ASAP 2460 analyzer. The pore size distributions and specific surface areas and were studied by Barrett-Joyner-Halenda model and Brunauer-Emmett-Teller (BET) equation, respectively. The morphologies of the products were examined by field-emission scanning electron microscopy (FE-SEM, Hitachi S4800) and transmission electron microscopy (TEM, Hitachi H-800).

## Electrochemical measurements

The electrochemical tests were conducted with coin cells (CR2032). Three different loadings of Fe<sub>2</sub>O<sub>3</sub>-NPCFs samples and pure NPCFs were directly used as the working electrodes. The density of the active material is about 1.5–1.8 mg cm<sup>-2</sup>. A lithium foil was used as the counter electrode, and Celgard 2400 was used as the separator. The electrolyte was LiPF<sub>6</sub> in ethylene carbonate/dimethyl carbonate/diethyl carbonate (EC/DMC/DEC, 1:1:1 vol %). In addition, the Fe<sub>2</sub>O<sub>3</sub> electrode was made by mixing active materials, Super-P carbon black and polyvinylidene fluoride (PVDF) with a weight ratio of 80:10:10. The coin cells were assembled in an argon-filled glove box (H<sub>2</sub>O, O<sub>2</sub> < 0.1 ppm, MBraun, Germany). Cyclic voltammetry (CV) and electrochemical impedance spectroscopy (EIS) were carried out by a CHI660D electrochemical workstation. CV was recorded at a scan rate of 0.1 mV s<sup>-1</sup> within the voltage range of 0.01–3.0 V, and EIS was recorded at open potential over the frequency range from 100 to 0.01 Hz. Galvanostatic charge/discharge measurements were performed on NEWARE CT-3008 instrument between 0.01 and 3.0 V vs Li/Li<sup>+</sup> at room temperature.

## Results and discussion

In this work, Fe<sub>2</sub>O<sub>3</sub> nanoparticles about 5 nm were prepared through a nonaqueous sol–gel method. In comparison with the complex aqueous sol–gel process, nonaqueous processes can enable the nanomaterials with good crystallinity and uniform morphologies [33]. The formation mechanism of Fe<sub>2</sub>O<sub>3</sub> nanoparticles during the sol process is depicted as follows:



In the following pyrolysis process, the gel molecules break down and change into Fe<sub>2</sub>O<sub>3</sub> nanoparticles. The XRD pattern of ZIF-8 is shown in Fig. S1a and the positions of reflection peaks are consistent with the simulated pattern, demonstrating that ZIF-8 is successfully prepared. Fig. S1b exhibits the XRD pattern of NPCFs and shows two broad humps at 2θ of about 28° and 43°, suggesting the amorphous

nature of carbon [34]. Figure 1a shows XRD patterns of Fe<sub>2</sub>O<sub>3</sub>/NPCFs composites. As can be seen, the diffraction peaks of three nanocomposites can be assigned to Fe<sub>2</sub>O<sub>3</sub> without any impurities (JCPDS 33-0664). The full XPS spectrum of Fe<sub>2</sub>O<sub>3</sub>/NPCFs-66.9% in Fig. 1b was employed to confirm that the composite is only composed of C, O, N and Fe elements. In addition, two distinct peaks located at 724.9 eV and 711.1 eV are observed in Fig. 1c, corresponding to Fe 2p<sub>1/2</sub> and Fe 2p<sub>3/2</sub> of Fe<sub>2</sub>O<sub>3</sub>, respectively [35, 36]. What is more, a broad satellite peak located at about 718.1 eV can further indicate it belongs to Fe<sub>2</sub>O<sub>3</sub>. Based on the XRD and XPS results, it can be confirmed that the Fe<sub>2</sub>O<sub>3</sub>/NPCFs composites have been synthesized successfully through this facile method. The flexible test results of the Fe<sub>2</sub>O<sub>3</sub>/NPCFs films are shown in Fig. 1d. A full film without any apparent defects in bending state can be seen. To further explore the flexibility of Fe<sub>2</sub>O<sub>3</sub>/NPCFs films, we attached the composites film on a pen by winding it closely. However, no obvious structural failure can be observed even after rolling, suggesting that the Fe<sub>2</sub>O<sub>3</sub>/NPCFs films have great potential for free-standing anodes with their outstanding flexibility.

The interfacial interaction in Fe<sub>2</sub>O<sub>3</sub>/NPCFs hybrids was investigated by Raman measurement, which has been testified a useful tool to observe the modification of carbon and their derivatives. As shown in Fig. 2a, Raman spectra of NPCFs show the regular D peak (ca. 1342 cm<sup>-1</sup>) and G peak (ca. 1573 cm<sup>-1</sup>). It is commonly accepted that the chemical link can change the electronic structures of carbon materials due to the change of hybridization of the carbon atoms. In addition, the charge transfer between carbon materials and nanocrystals can cause the shift of the G peak [37, 38]. Therefore, Raman measurement is an ideal probe to investigate the interaction between Fe<sub>2</sub>O<sub>3</sub> and NPCFs. In this work, the observed shift by 11 cm<sup>-1</sup> from 1573 (NPCFs) to 1584 cm<sup>-1</sup> (Fe<sub>2</sub>O<sub>3</sub>/NPCFs composite) demonstrates the presence of a charge transfer between NPCFs and Fe<sub>2</sub>O<sub>3</sub> nanoparticles. The interaction can also be confirmed by TG measurement in the air. Because the types of contact, such as loose contact and tight contact, between the metal oxide catalysts and carbon materials are the crucial factor for oxidation reactivity of carbon materials [39]. As shown in Fig. 2b, the oxidation temperature for Fe<sub>2</sub>O<sub>3</sub>/NPCFs composite is about 280 °C, while NPCFs is about 470 °C. Such a large drop in temperature suggested that there was a tight

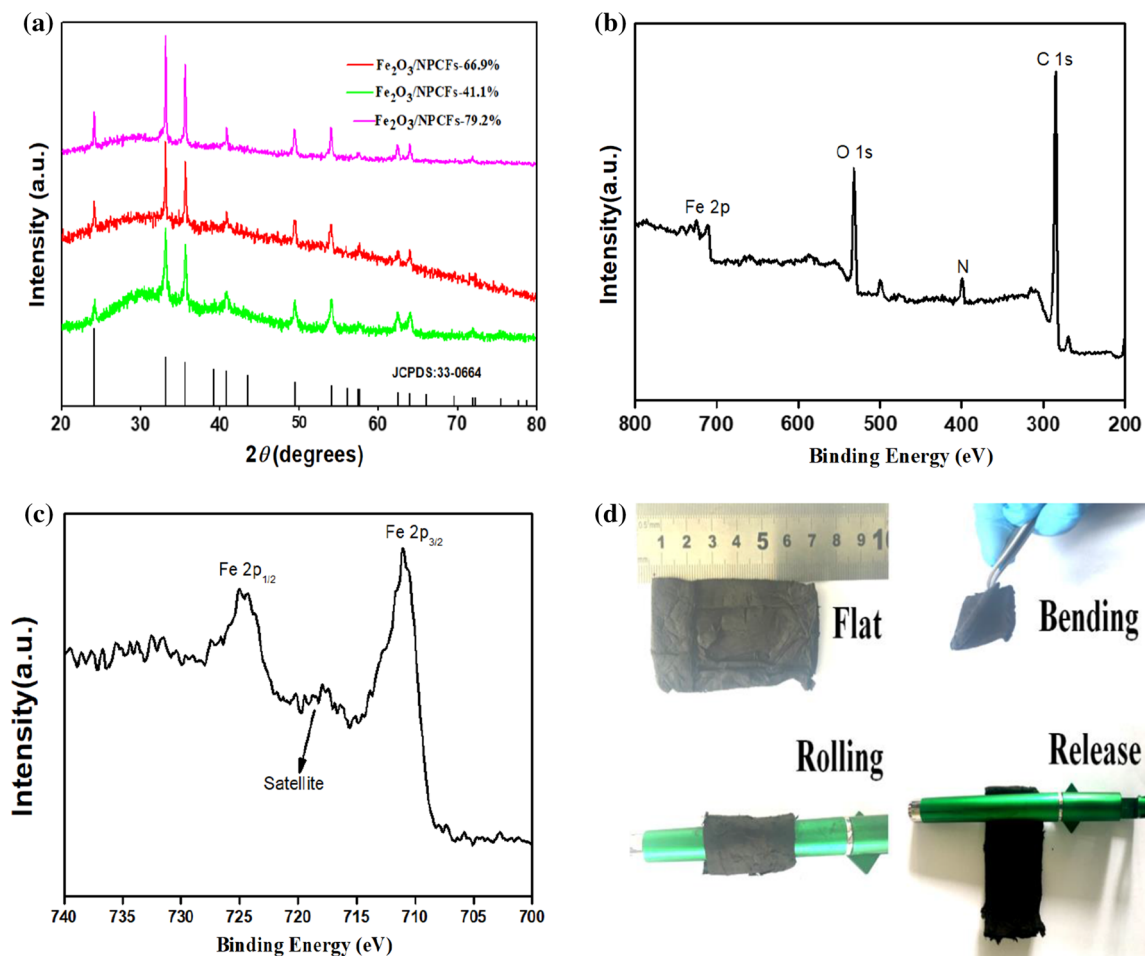


**Figure 1** a XRD patterns of Fe<sub>2</sub>O<sub>3</sub>/NPCFs composites. b Full XPS spectrum of Fe<sub>2</sub>O<sub>3</sub>/NPCFs-66.9%. c High-resolution XPS spectrum of Fe 2p in Fe<sub>2</sub>O<sub>3</sub>/NPCFs-66.9% d Digital photographs showing the flexibility of the Fe<sub>2</sub>O<sub>3</sub>/NPCFs-66.9% product.

contact between Fe<sub>2</sub>O<sub>3</sub> and NPCFs. In addition, the Fe<sub>2</sub>O<sub>3</sub>/NPCFs composites exhibit a total weight loss of about 33.1, 20.8 and 58.9% between 280 and 400 °C, which is attributed to the evaporation of adsorbed water molecules and the combustion of NPCFs (Fig. S2a). Therefore, the content of Fe<sub>2</sub>O<sub>3</sub> in the composites is 66.9, 79.2 and 41.1% for Fe<sub>2</sub>O<sub>3</sub>/NPCFs-66.9%, Fe<sub>2</sub>O<sub>3</sub>/NPCFs-41.1% and Fe<sub>2</sub>O<sub>3</sub>/NPCFs-79.2% products. The binding between NPCFs and Fe<sub>2</sub>O<sub>3</sub> was further identified by XPS. Figure S2b exhibits the full-scan XPS spectra of NPCFs, suggesting the existence of C, N, and O. In Fig. 2c, the C 1s spectra of the NPCFs was deconvoluted into four peaks, which corresponds to O–C=O, C–O, C–N and C–C [40]. Compared with NPCFs, the peak intensity of C–O and O–C=O becomes lower after incorporating Fe<sub>2</sub>O<sub>3</sub> nanoparticles into NPCFs (Fig. 2d). It can be attributed to the new oxygen-containing groups and some O–C=O groups on the NPCFs were broken down to

form the Fe–O–C bonds during the in situ nonaqueous sol–gel process, respectively [41]. Furthermore, high-resolution XPS spectra of O 1s in Fig. 2e, f can also prove the conclusion. The new peak at 531.3 eV can be attributed to the Fe–O–C bond between Fe<sub>2</sub>O<sub>3</sub> and NPCFs. It can also be confirmed from the previous literature that the binding energy of O 1s in Fe–O–C bond can exist in the line of 531–533 eV [42]. All of this analysis confirmed the conclusion that the Fe–O–C bonds were formed between NPCFs and Fe<sub>2</sub>O<sub>3</sub>. The strong interfacial interaction can not only enhance the structural stability of the whole electrode, but also can withstand the volume expansion and agglomeration of Fe<sub>2</sub>O<sub>3</sub> nanoparticles during cycling.

The morphology and microstructure of the as-prepared NPCFs and Fe<sub>2</sub>O<sub>3</sub>/NPCFs hybrids were characterized by FE-SEM. As shown in Fig. 3a–c, the obtained NPCFs present a 1D structure with a

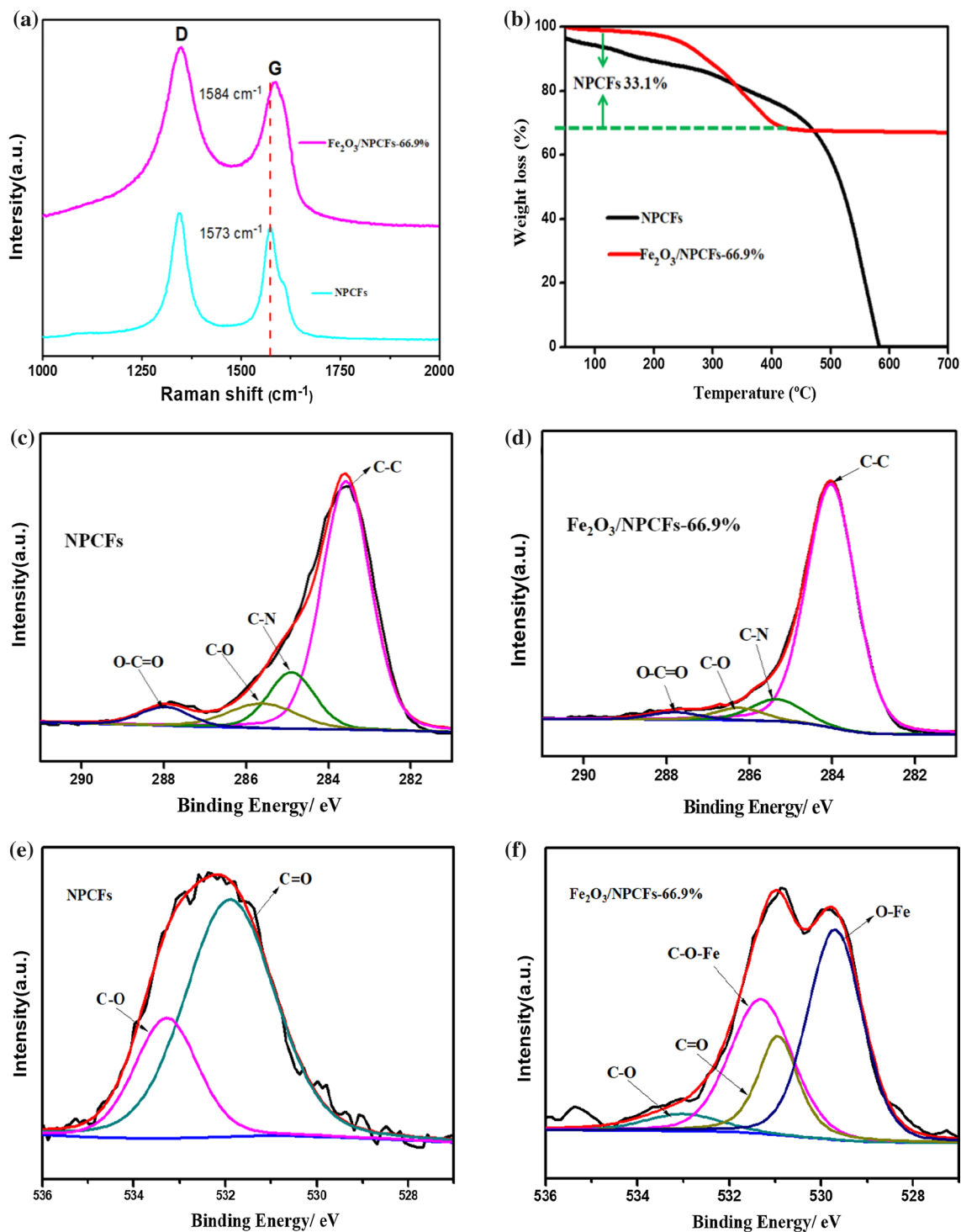


**Figure 2** Raman spectra (a) and TG curves (b) of NPCFs and Fe<sub>2</sub>O<sub>3</sub>/NPCFs-66.9%. High-resolution XPS spectra of C 1s (c, d) and O 1s (e, f) of NPCFs and Fe<sub>2</sub>O<sub>3</sub>/NPCFs-66.9%.

diameter of about 200 nm and smooth surface. Many typical mesoporous formed by the carbonization of ZIF-8 nanoparticles can also be observed. In addition, NPCFs weave into an interconnected network with

an interspace of about hundreds of nanometers, which can provide efficient channels for electrolyte penetration and electron transfer. The as-synthesized ZIF-8 is also characterized by SEM, and the

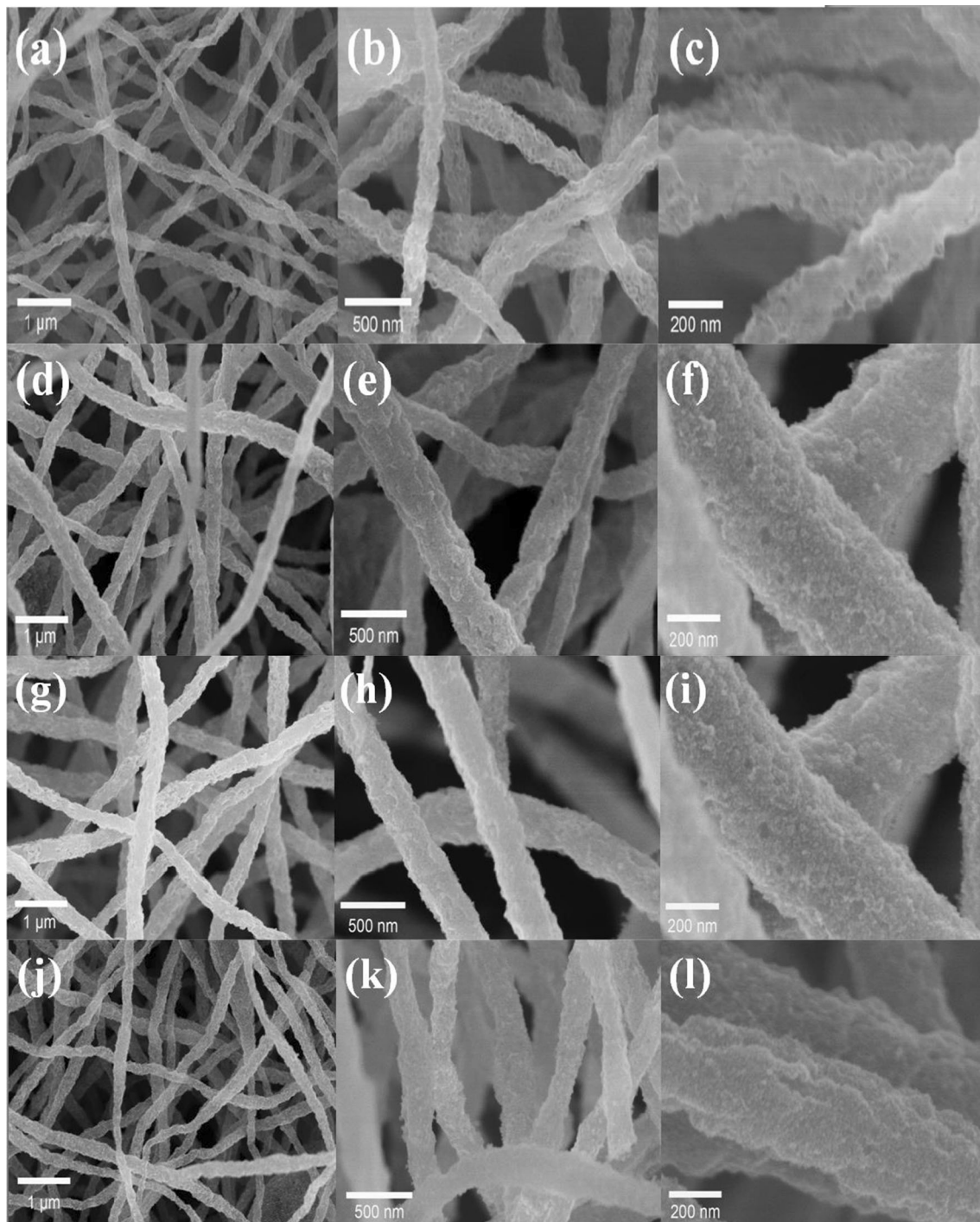


**Figure 3** SEM images of NPCFs (a–c),  $\text{Fe}_2\text{O}_3/\text{NPCFs}$ -41.1% (d–f),  $\text{Fe}_2\text{O}_3/\text{NPCFs}$ -66.9% (g–i) and  $\text{Fe}_2\text{O}_3/\text{NPCFs}$ -79.2% (j–l).

crystalline size is about 50 nm (Fig. S3). From Fig. 3d–l, it is more clearly observed that no obvious morphological changes in the  $\text{Fe}_2\text{O}_3/\text{NPCFs}$  composites after decorating with  $\text{Fe}_2\text{O}_3$  nanoparticles, still showing 1D architecture. However, the roughness of the three NPCFs surfaces increases with the increase

in  $\text{Fe}_2\text{O}_3$  loading from 41.1 to 79.2%. When the  $\text{Fe}_2\text{O}_3$  content was increased to 79.2%, the nanoparticles will agglomerate on the surface of NPCFs due to the lack of sufficient space for infiltration. Moreover, it would affect the transfer of  $\text{Li}^+$  across the electrolyte and  $\text{Fe}_2\text{O}_3/\text{NPCFs}$  interface. Therefore, exploring the

mass ratio between  $\text{Fe}_2\text{O}_3$  and NPCFs to an optimal composition is crucial for getting superior electrochemical performance.

The high-resolution TEM image (HRTEM) of  $\text{Fe}_2\text{O}_3$  counterpart is shown in Fig. 4a. The sizes of the  $\text{Fe}_2\text{O}_3$  nanoparticles are about 5 nm, which is much smaller than that of previous reports [35, 43]. However, the  $\text{Fe}_2\text{O}_3$  nanoparticles are clustered together due to the lack of the NPCFs matrix. The TEM images in Fig. 4b, c reveal that  $\text{Fe}_2\text{O}_3$  nanoparticles are distributed in the hollow carbon cages without agglomeration. In addition, rich mesopores existed in the 1D structure can also be observed clearly. These mesopores can not only shorten the  $\text{Li}^+$  diffusion distance, insure the efficient  $\text{Li}^+$  flux, but also can accommodate the

possible volume change of  $\text{Fe}_2\text{O}_3$  nanoparticles during cycling. The HRTEM image in Fig. 4f showed that the interplanar spacing was 0.27 nm corresponding to (104) planes of tetragonal  $\text{Fe}_2\text{O}_3$ . Elemental mapping test was used to determine the distribution of  $\text{Fe}_2\text{O}_3$  nanoparticles in the  $\text{Fe}_2\text{O}_3/\text{NPCFs}$ -66.9% sample. As shown in Fig. 4e–i, a highly uniform distribution of C, N, Fe, and O species can be seen, further confirming that  $\text{Fe}_2\text{O}_3$  nanoparticles evenly distributed in the NPCFs matrix.

The porous and textural properties of the as-prepared NPCFs and  $\text{Fe}_2\text{O}_3/\text{NPCFs}$ -66.9% are further investigated by nitrogen adsorption/desorption analyses. As shown in Fig. 5, these two isotherms exhibit type IV isotherms with distinct hysteresis

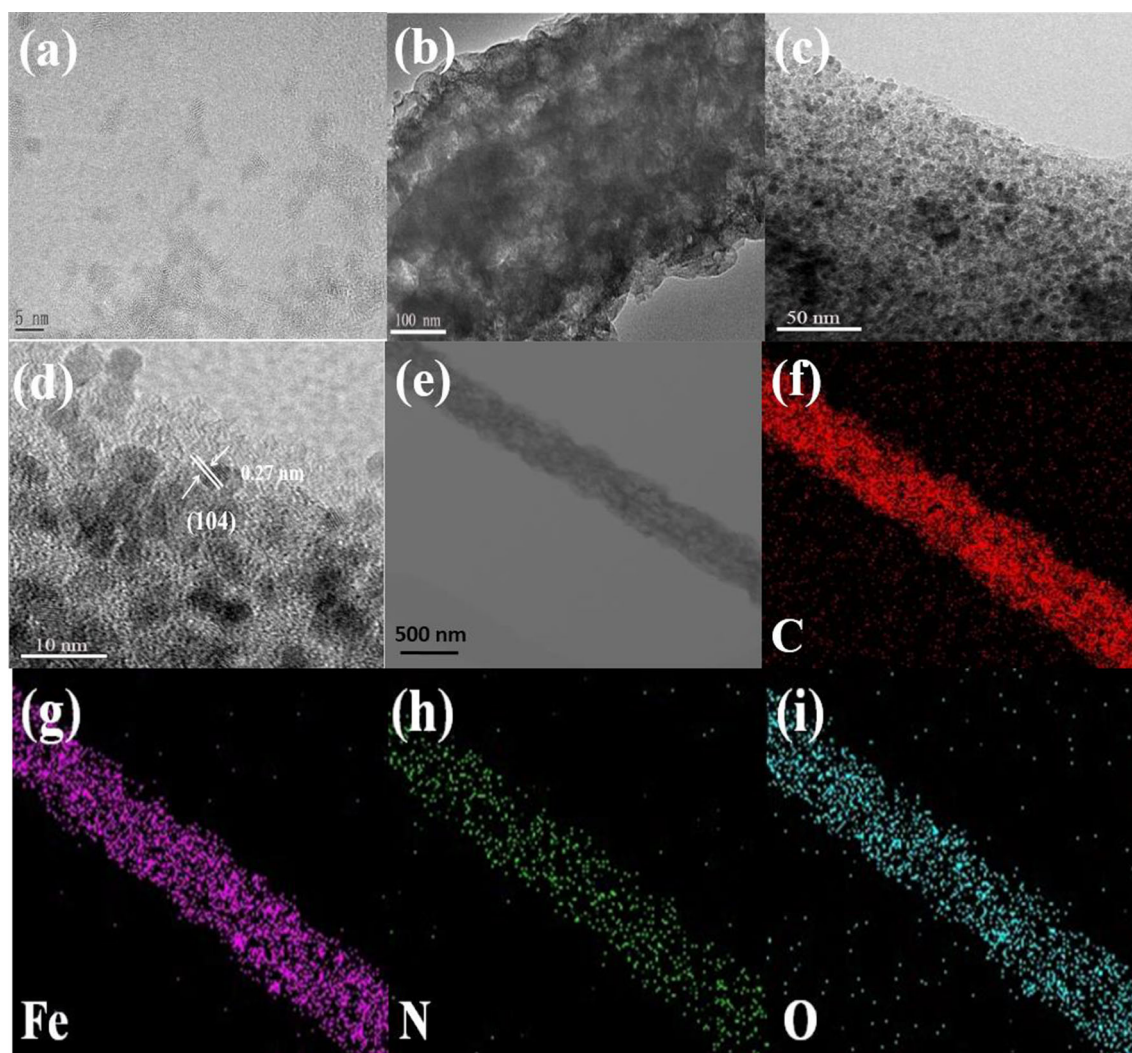


**Figure 4** High-resolution TEM images of  $\text{Fe}_2\text{O}_3$  (a). TEM (b, c) and high-resolution TEM (d) images of  $\text{Fe}_2\text{O}_3/\text{NPCFs}$ -66.9% hybrid. TEM image of  $\text{Fe}_2\text{O}_3/\text{NPCFs}$ -66.9% (e) and its

corresponding element mapping of C (f), Fe (g), N (h), O (i). The inset of d selected area electron diffraction pattern of  $\text{Fe}_2\text{O}_3/\text{NPCFs}$ -66.9% hybrid.



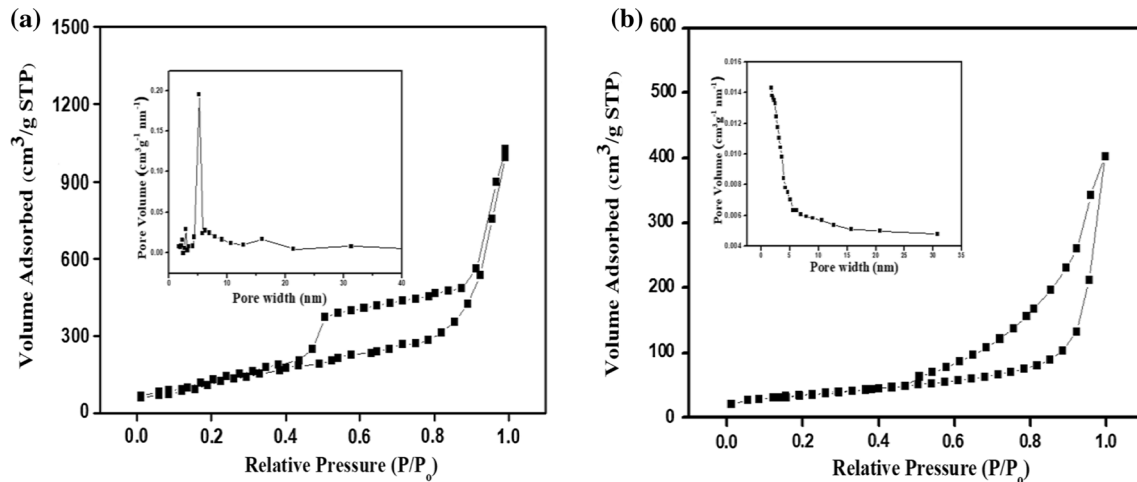
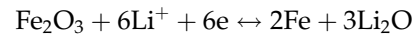


**Figure 5** Nitrogen adsorption/desorption isotherms and the corresponding pore size distribution curves of NPCFs (a) and Fe<sub>2</sub>O<sub>3</sub>/NPCFs-66.9% (b).

loops in the medium to high relative pressure, which illustrates the mesoporous feature of the two materials [44]. The specific surface areas of NPCFs, Fe<sub>2</sub>O<sub>3</sub>/NPCFs-66.9% and bare Fe<sub>2</sub>O<sub>3</sub> (Fig. S4) are 424.7, 125.4 and 10.1 m<sup>2</sup> g<sup>-1</sup>, respectively. The corresponding pore size distribution curves indicate that mesopores dominate in these samples. The porous structure in the bare Fe<sub>2</sub>O<sub>3</sub> may be associated with the textural mesoporosity between individual particles in the aggregates. The large specific surface areas and the meso-sized transporting pores of Fe<sub>2</sub>O<sub>3</sub>/NPCFs-66.9% can not only promote Li ions into the electrode material, but also increase the contact areas between the active materials and electrolyte.

The electrochemical behavior of the Fe<sub>2</sub>O<sub>3</sub>/NPCFs-66.9% material was examined by cyclic voltammetry (CV) at a scan rate of 0.1 mV s<sup>-1</sup> in the 0.01–3.0 V, and the curves are shown in Fig. 6a. In the first cathodic sweep, a weak peak at 1.56 V is attributed to lithium intercalation in the crystal structure of Fe<sub>2</sub>O<sub>3</sub> nanoparticles. Another main cathodic peak at 0.66 V is assigned to the stepwise reduction of Fe<sup>3+</sup> to Fe<sup>2+</sup> and the complete reduction of Fe<sup>2+</sup> to Fe<sup>0</sup> as well as the formation of a solid electrolyte interface (SEI) layer because of the degradation of the electrolyte [45, 46]. In the anodic process, a broad peak centered at about 1.6 V is corresponded to the oxidation of Fe<sup>0</sup> to Fe<sup>3+</sup> [47]. In addition, a long tail (green elliptical region) at between 0.25 and 0.01 V can be observed in the CV curves, which is corresponded to the insertion of Li ions into the NPCFs matrix [48]. Moreover, the curves almost overlapped in the following cycles,

suggesting the superior reversibility of the Fe<sub>2</sub>O<sub>3</sub>/NPCFs-66.9% electrode. The electrochemical reaction mechanism of the electrode can be described by the following equation [46]:



As a comparison, the CV curves of Fe<sub>2</sub>O<sub>3</sub> anode are shown in Fig. S5. The shape is consistent with the Fe<sub>2</sub>O<sub>3</sub>/NPCFs-66.9% electrode, suggesting that the similar electrochemical reactions have happened in these two electrodes during lithium insertion/extraction processes.

The first five galvanostatic charge/discharge curves of Fe<sub>2</sub>O<sub>3</sub> and Fe<sub>2</sub>O<sub>3</sub>/NPCFs-66.9% anodes tested at 50 mA g<sup>-1</sup> are shown in Fig. 6b, c, respectively. In the first discharge curves, Fe<sub>2</sub>O<sub>3</sub> and Fe<sub>2</sub>O<sub>3</sub>/NPCFs-66.9% anodes show two similar potential plateaus at about 1.6 and 0.7 V, which are caused by lithium inserting into crystalline structure of Fe<sub>2</sub>O<sub>3</sub>, and the reduction of Fe<sup>3+</sup> to Fe<sup>0</sup> by metallic Li as well as the formation of SEI film. The reverse conversion reaction from Fe<sup>0</sup> to Fe<sup>3+</sup> results in the sloping plateau from 1.50 to 2.0 V. All these observations are consistent with the CV results. The initial discharge and charge capacities of Fe<sub>2</sub>O<sub>3</sub>/NPCFs-66.9% electrode are 1778 and 1323 mA h g<sup>-1</sup> with a Coulombic efficiency (CE) of 74.4%, which is higher than that of Fe<sub>2</sub>O<sub>3</sub> nanoparticles (48.9%). The large capacity loss can be attributed to the formation of SEI film and the irreversible decomposition of electrolyte [49, 50]. In the following four cycles, the charge–discharge curves of the Fe<sub>2</sub>O<sub>3</sub>/NPCFs-66.9% electrode almost

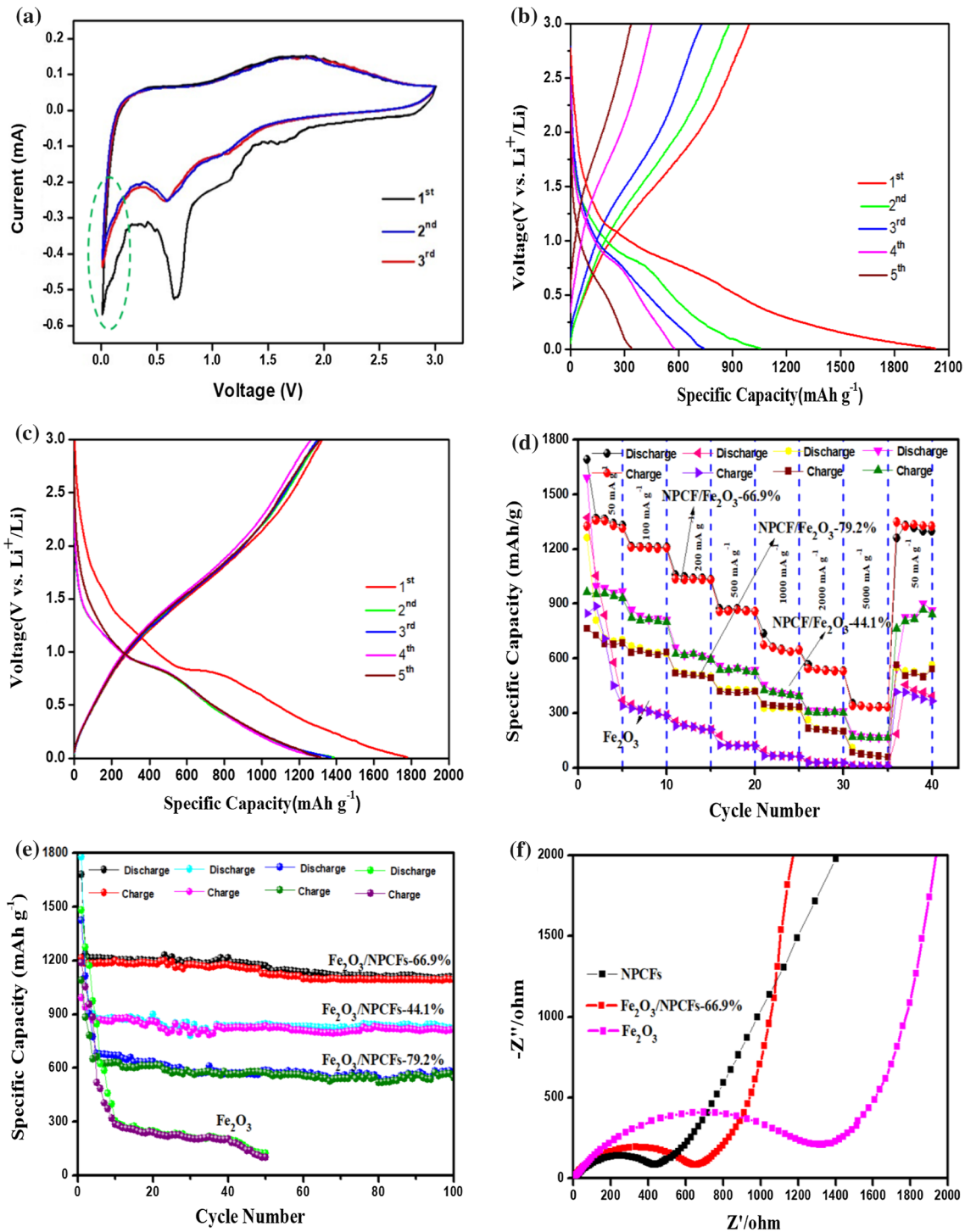


**Figure 6** a CV curves of Fe<sub>2</sub>O<sub>3</sub>/NPCFs-66.9%. Charge-discharge profiles of Fe<sub>2</sub>O<sub>3</sub> (b) and Fe<sub>2</sub>O<sub>3</sub>/NPCFs-66.9% (c) at 50 mA g<sup>-1</sup>. d Rate performance curves Fe<sub>2</sub>O<sub>3</sub> and Fe<sub>2</sub>O<sub>3</sub>/NPCFs

composites. e Cycling performance of Fe<sub>2</sub>O<sub>3</sub> and Fe<sub>2</sub>O<sub>3</sub>/NPCFs at 100 mA g<sup>-1</sup>. f Electrochemical impedance spectra of Fe<sub>2</sub>O<sub>3</sub>, NPCFs and Fe<sub>2</sub>O<sub>3</sub>/NPCFs-66.9% electrodes.

overlap, demonstrating better cyclic stability. (1313 mA h g<sup>-1</sup> at the fifth cycles) However, for the Fe<sub>2</sub>O<sub>3</sub> electrode, the specific capacity is dramatically reduced due to the lack of NPCFs matrix to

accommodate the volume expansion during cycling. (339 mA h g<sup>-1</sup> at the fifth cycles).

Figure 6d exhibits the rate performance of the Fe<sub>2</sub>O<sub>3</sub> and Fe<sub>2</sub>O<sub>3</sub>/NPCFs electrodes at different

current densities from 50 to 5000 mA g<sup>-1</sup> and 5 cycles for each step. We can observe that the Fe<sub>2</sub>O<sub>3</sub> electrode delivers fast capacity fading compared with Fe<sub>2</sub>O<sub>3</sub>/NPCFs electrodes. The discharge specific capacity decreases to 8.4 mA h g<sup>-1</sup> at 5000 mA g<sup>-1</sup>. When the current density returns to 50 mA g<sup>-1</sup>, the capacity can only recover to 224 mA h g<sup>-1</sup>. On the contrary, all the three Fe<sub>2</sub>O<sub>3</sub>/NPCFs electrodes show better rate performance than Fe<sub>2</sub>O<sub>3</sub> bulk electrode and the Fe<sub>2</sub>O<sub>3</sub>/NPCFs-66.9% electrode has the highest reversible capacity at different current densities. The average discharge capacities (removing the first cycle) of Fe<sub>2</sub>O<sub>3</sub>/NPCFs-66.9% electrode are 1351, 1211, 1044, 866, 666, 540, and 337 mA h g<sup>-1</sup> at a current density from 50 to 5000 mA g<sup>-1</sup>, respectively. Notably, when the current density returns to 50 mA g<sup>-1</sup>, the discharge specific capacities can recover to 1310 mA h g<sup>-1</sup>, corresponding to a nearly 97% capacity retention. This implies that the NPCFs matrix plays an important role to overcome the intrinsic disadvantages of Fe<sub>2</sub>O<sub>3</sub> bulk materials. In addition, the superior rate cycling capability of Fe<sub>2</sub>O<sub>3</sub>/NPCFs composites is mainly attributed to the stability of 1D structure, improved electronic conductivity and the strong interfacial interaction Fe–O–C bond between Fe<sub>2</sub>O<sub>3</sub> nanoparticles and NPCFs.

The cycling stability of the Fe<sub>2</sub>O<sub>3</sub> and Fe<sub>2</sub>O<sub>3</sub>/NPCFs electrodes were investigated by galvanostatic charge–discharge processes between 0.01 and 3.0 V at 100 mA g<sup>-1</sup> for 100 cycles, as shown in Fig. 6e. Fe<sub>2</sub>O<sub>3</sub> electrode exhibits a high initial capacity, whereas Fe<sub>2</sub>O<sub>3</sub>/NPCFs a rapid decrease. When the stability test reached 50 cycles, the specific capacity decreased from 1482 to 123 mA h g<sup>-1</sup> (only 8% retained). The main reason for the rapid capacity fading is the pulverization of the electrode caused by the large volume expansion of Fe<sub>2</sub>O<sub>3</sub> nanoparticles during the charge–discharge processes. On the contrary, the capacity of the Fe<sub>2</sub>O<sub>3</sub>/NPCFs electrodes leveled off from the 40th cycle. The reversible capacities after 100 cycles are about 1106, 820, and 563 mA h g<sup>-1</sup> for Fe<sub>2</sub>O<sub>3</sub>/NPCFs-66.9%, Fe<sub>2</sub>O<sub>3</sub>/NPCFs-44.1% and Fe<sub>2</sub>O<sub>3</sub>/NPCFs-79.2%, respectively. Three reasons could be contributed to the significantly increased electrochemical performance: (1) The small size of Fe<sub>2</sub>O<sub>3</sub> nanoparticles about 5 nm can shorten the diffusion distance of Li ions and enhance the reaction efficiency. (2) The N-doping of porous carbon fibers can increase the conductivity and provide lots of active sites, thus realizing the rapid charge transfer

and the high reversibility capacity. (3) The robust 1D structure of NPCFs and the strong interfacial interaction Fe–O–C bond can not only restrain the aggregation of Fe<sub>2</sub>O<sub>3</sub> nanoparticles, but also can accommodate the volume change to effectively maintain the integrity of the whole electrode during the long-term cycles. In addition, when the mass ratio of Fe<sub>2</sub>O<sub>3</sub> is 66.9 wt%, the Fe<sub>2</sub>O<sub>3</sub>/NPCFs-66.9% composite exhibits the best cycling stability, suggesting an optimized mass ratio is also important for improving the electrochemical performance. Moreover, the Fe<sub>2</sub>O<sub>3</sub>/NPCFs-79.2% electrode shows a lower rate performance and cycling stability as compared with Fe<sub>2</sub>O<sub>3</sub>/NPCFs-66.9%, Fe<sub>2</sub>O<sub>3</sub>/NPCFs-44.1%. This phenomenon can be attributed to the reduced electrical conductivity and porous architecture for the composite. Because pure Fe<sub>2</sub>O<sub>3</sub> material has a relatively low intrinsic electrical conductivity, the conductivity of the whole material decreases drastically as the loading density increases. In addition, when the mass ratio was further increased from 66.9 to 79.2%, most of the Fe<sub>2</sub>O<sub>3</sub> nanoparticles exposed on the outer surface of the NPCFs network, which was consistent with observation by SEM in Fig. 3i, j. These nanoparticles blocked the void space of NPCFs matrix and hindered the infiltration of electrolyte into the whole Fe<sub>2</sub>O<sub>3</sub>/NPCFs hybrids. Therefore, the Fe<sub>2</sub>O<sub>3</sub>/NPCFs-79.2% electrode exhibited a poor electrochemical performance compared with Fe<sub>2</sub>O<sub>3</sub>/NPCFs-66.9%, Fe<sub>2</sub>O<sub>3</sub>/NPCFs-44.1%.

To reveal the charge transfer kinetics of the Fe<sub>2</sub>O<sub>3</sub>/NPCFs composites, EIS measurement was performed (Fig. 6f). Apparently, each plot consists of one compressed semicircle in the high-middle frequency regions that is assigned to the charge transfer resistance ( $R_{ct}$ ) and a straight sloping line in the low-frequency region corresponding to the Warburg impedance ( $Z_W$ ), which is influenced by ion diffusion [51, 52]. The  $R_{ct}$  of the Fe<sub>2</sub>O<sub>3</sub>/NPCFs-66.9% electrode is 628  $\Omega$ , which is higher than that of the NPCFs (423  $\Omega$ ) and much lower than Fe<sub>2</sub>O<sub>3</sub> (1335  $\Omega$ ) electrodes. The smaller  $R_{ct}$  value of Fe<sub>2</sub>O<sub>3</sub>/NPCFs-66.9% hybrid means that it has a rapid electron transport rate during the electrochemical lithium insertion/extraction reaction. The excellent electrical conductivity and the unique architecture of the composite collectively contribute to the superior electrochemical performance.

The morphologies of the Fe<sub>2</sub>O<sub>3</sub>/NPCFs-44.1%, Fe<sub>2</sub>O<sub>3</sub>/NPCFs-66.9% and Fe<sub>2</sub>O<sub>3</sub>/NPCFs-79.2%

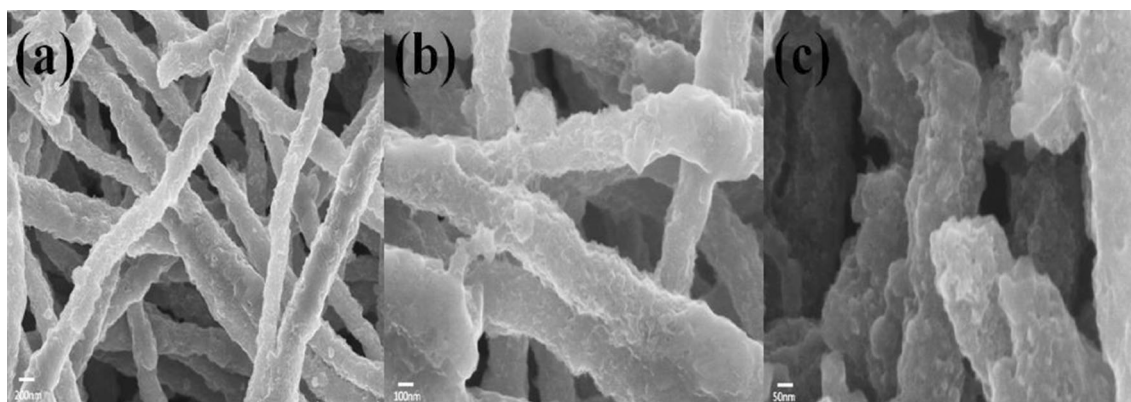


**Figure 7** SEM images of  $\text{Fe}_2\text{O}_3/\text{NPCFs}$ -44.1% (a),  $\text{Fe}_2\text{O}_3/\text{NPCFs}$ -66.9% (b) and  $\text{Fe}_2\text{O}_3/\text{NPCFs}$ -79.2% (c) electrodes after 100 charge/discharge cycles at  $100 \text{ mA g}^{-1}$ .

electrodes after 100 cycles were further examined by SEM and shown in Fig. 7a–c, respectively. It can be observed clearly that the 1D architecture of NPCFs was preserved without the obvious damage in Fig. 7a, b. However, the structure of NPCFs was almost destroyed, and a lot of agglomerations can be found easily. This phenomenon may be caused by the increase in  $\text{Fe}_2\text{O}_3$  content. Because of the lack of a NPCFs matrix to accommodate the serious volume expansion of excess  $\text{Fe}_2\text{O}_3$  nanoparticles during  $\text{Li}^+$  intercalation/deintercalation process, this can result in structural distortion and crack. These results are in good agreement with the cycling performance tests.  $\text{Fe}_2\text{O}_3/\text{NPCFs}$ -66.9% and  $\text{Fe}_2\text{O}_3/\text{NPCFs}$ -44.1% electrodes exhibit higher reversible specific capacity than  $\text{Fe}_2\text{O}_3/\text{NPCFs}$ -79.2% electrode.

## Conclusion

In summary, free-standing and flexible electrode  $\text{Fe}_2\text{O}_3/\text{NPCFs}$  were successfully prepared through electrospinning technology and nonaqueous sol–gel process, followed by pyrolysis. The resultant 1D NPCFs were formed of mesopores and macropores and exhibited a large surface area and high porosity. We also explored the impact of  $\text{Fe}_2\text{O}_3$  loading amount on electrochemical performance in this paper and the optimal content in  $\text{Fe}_2\text{O}_3/\text{NPCFs}$  hybrids is 66.9 wt%. In addition, the results of TG curves, Raman spectra, XPS spectra indicated that the strongly interfacial interaction Fe–O–C bonds were formed between NPCFs and  $\text{Fe}_2\text{O}_3$ . When used as an anode material for LIBs, the  $\text{Fe}_2\text{O}_3/\text{NPCFs}$ -66.9% hybrid exhibited the smaller size of  $\text{Fe}_2\text{O}_3$  nanoparticles (about 5 nm), 1D architecture and excellent

electrical conductivity of NPCFs as well as the strong interfacial interaction. Moreover, the convenient preparation processes, natural abundance raw materials and low cost exhibit a promising application for  $\text{Fe}_2\text{O}_3/\text{NPCFs}$ -66.9% composite as electrode material for LIBs.

## Acknowledgements

This work was financially supported by the Shanghai University of Engineering Science Innovation Fund for Graduate Students (17KY0405).

**Electronic supplementary material:** The online version of this article (<https://doi.org/10.1007/s10853-019-03330-0>) contains supplementary material, which is available to authorized users.

## References

- [1] Zhang Y, Zhao Y, Ren J, Weng W, Peng H (2016) Advances in wearable fiber-shaped lithium-ion batteries. *Adv Mater* 28:4524–4531. <https://doi.org/10.1002/adma.201503891>
- [2] Nitta N, Wu F, Lee JT, Yushin G (2015) Li-ion battery materials: present and future. *Mater Today* 18:252–264. <https://doi.org/10.1016/j.mattod.2014.10.040>
- [3] Larcher D, Tarascon JM (2015) Towards greener and more sustainable batteries for electrical energy storage. *Nat Chem* 7:19–29. <https://doi.org/10.1038/nchem.2085>
- [4] Ji L, Lin Z, Alcoutlabi M, Zhang X (2011) Recent developments in nanostructured anode materials for rechargeable lithium-ion batteries. *Energy Environ Sci* 4:2682–2699. <https://doi.org/10.1039/c0ee00699h>

- [5] Ji L, Rao M, Zheng H et al (2011) Graphene oxide as a Sulfur immobilizer in high performance lithium/sulfur cells. *J Am Chem Soc* 133:18522–18525. <https://doi.org/10.1021/ja206955k>
- [6] Li W, Wu J, Chen Y, Wang X, Zhou R, Chen S, Guo Q, Hou H, Song Y (2015) Hollow Nitrogen-doped Fe<sub>3</sub>O<sub>4</sub>/Carbon nanocages with hierarchical porosities as anode materials for lithium-ion batteries. *Electrochim Acta* 186:50–57. <https://doi.org/10.1016/j.electacta.2015.10.134>
- [7] Keppeler M, Shen N, Nageswaran S, Srinivasan M (2016) Synthesis of  $\alpha$ -Fe<sub>2</sub>O<sub>3</sub>/Carbon nanocomposites as high capacity electrodes for next generation lithium ion batteries: a review. *J Mater Chem A* 4:18223–18239. <https://doi.org/10.1039/c6ta08456g>
- [8] Li J, Dahn HM, Krause LJ, Le D-B, Dahn JR (2008) Impact of binder choice on the performance of  $\alpha$ -Fe<sub>2</sub>O<sub>3</sub> as a negative electrode. *J Electrochem Soc* 155:A812–A816. <https://doi.org/10.1149/1.2969433>
- [9] Larcher D, Masquelier C, Bonnin D et al (2003) Effect of particle size on lithium intercalation into  $\alpha$ -Fe<sub>2</sub>O<sub>3</sub>. *J Electrochem Soc* 150:A133–A139. <https://doi.org/10.1149/1.1528941>
- [10] Larcher D, Bonnin D, Cortes R, Rivals I, Personnaz L, Tarascon JM (2003) Combined XRD, EXAFS, and Mössbauer studies of the reduction by lithium of  $\alpha$ -Fe<sub>2</sub>O<sub>3</sub> with various particle sizes. *J Electrochem Soc* 150:A1643–A1650. <https://doi.org/10.1149/1.1622959>
- [11] Wang Z, Luan D, Madhavi S, Hu Y, Lou X (2012) Assembling carbon-coated  $\alpha$ -Fe<sub>2</sub>O<sub>3</sub> hollow nanohorns on the CNT backbone for superior lithium storage capability. *Energy Environ Sci* 5:5252–5256. <https://doi.org/10.1039/c1ee02831f>
- [12] Luo D, Lin F, Xiao W, Zhu W (2017) Synthesis and electrochemical performance of  $\alpha$ -Fe<sub>2</sub>O<sub>3</sub>@carbon aerogel composite as an anode material for Li-ion batteries. *Ceram Int* 43:2051–2056. <https://doi.org/10.1016/j.ceramint.2016.10.178>
- [13] Ji L, Toprakci O, Alcoutlabi M et al (2012)  $\alpha$ -Fe<sub>2</sub>O<sub>3</sub> Nanoparticle-loaded carbon nanofibers as stable and high-capacity anodes for rechargeable lithium-ion batteries. *ACS Appl Mater Interfaces* 4:2672–2679. <https://doi.org/10.1021/am300333s>
- [14] Zhu J, Zhu T, Zhou X et al (2011) Facile synthesis of metal oxide/reduced graphene oxide hybrids with high lithium storage capacity and stable cyclability. *Nanoscale* 3:1084–1089. <https://doi.org/10.1039/c0nr00744g>
- [15] Liu L, Yang X, Lv C et al (2016) Seaweed-derived route to Fe<sub>2</sub>O<sub>3</sub> hollow nanoparticles/N-doped graphene aerogels with high lithium ion storage performance. *ACS Appl Mater Interfaces* 8:7047–7053. <https://doi.org/10.1021/acsami.5b12427>
- [16] Xiao W, Wang Z, Guo H et al (2013) Fe<sub>2</sub>O<sub>3</sub> particles enwrapped by graphene with excellent cyclability and rate capability as anode materials for lithium ion batteries. *Appl Surf Sci* 266:148–154. <https://doi.org/10.1016/j.apsusc.2012.11.118>
- [17] Niu Z, Chen J, Hng HH, Ma J, Chen X (2012) A leavening strategy to prepare reduced graphene oxide foams. *Adv Mater* 24:4144–4150. <https://doi.org/10.1002/adma.201200197>
- [18] Wang X, Zhang M, Liu E et al (2016) Three-dimensional core-shell Fe<sub>2</sub>O<sub>3</sub>@ carbon/carbon cloth as binder-free anode for the high-performance lithium-ion batteries. *Appl Surf Sci* 390:350–356. <https://doi.org/10.1016/j.apsusc.2016.08.112>
- [19] Park Y, Oh M, Park JS et al (2015) Electrochemically deposited Fe<sub>2</sub>O<sub>3</sub> nanorods on carbon nanofibers for free-standing anodes of lithium-ion batteries. *Carbon* 94:9–17. <https://doi.org/10.1016/j.carbon.2015.06.031>
- [20] Zhang H, Zhou L, Noonan O, Martin DJ, Whittaker AK, Yu C (2014) Tailoring the void size of iron oxide@carbon yolk-shell structure for optimized lithium storage. *Adv Funct Mater* 24:4337–4342. <https://doi.org/10.1002/adfm.201400178>
- [21] Zhu Q, Xu Q (2014) Metal-organic framework composites. *Chem Soc Rev* 43:5468–5512. <https://doi.org/10.1039/c3cs60472a>
- [22] Sun X, Huang H, Wang C, Liu Y, Bu X (2014) Effective Co<sub>x</sub>S<sub>y</sub> HER electrocatalysts fabricated in situ sulfuring of metal-organic framework. *ChemElectroChem* 5(23):3639–3644. <https://doi.org/10.1002/celec.201801238>
- [23] Wu J, Song Y, Zhou R, Chen S, Li Z, Hou H, Wang L (2015) Zn-Fe-ZIF-derived porous ZnFe<sub>2</sub>O<sub>4</sub>/C@NCNTs nanocomposites as anode for lithium-ion batteries. *J Mater Chem A* 3:7793–7798. <https://doi.org/10.1039/c5ta00805k>
- [24] Chen Y, Zheng L, Fu Y, Zhou R, Song Y, Chen S (2016) MOF-derived Fe<sub>3</sub>O<sub>4</sub>/carbon octahedral nanostructures with enhanced performance as anode materials for lithium-ion batteries. *RSC Adv* 6:85917–85923. <https://doi.org/10.1039/c6ra19041c>
- [25] Kong L, Zhu J, Shuang W, Bu X (2018) Nitrogen-doped wrinkled carbon foils derived from MOF nanosheets for superior sodium storage. *Adv Energy Mater* 8:1801515. <https://doi.org/10.1002/aenm.201801515>
- [26] Zhong M, He W, Wei S, Liu Y, Hu T, Bu X (2018) Metal-organic framework derived core-shell Co/Co<sub>3</sub>O<sub>4</sub>@N-C nanocomposites as high performance anode materials for lithium ion batteries. *Inorg Chem* 57:4620–4628. <https://doi.org/10.1021/acs.inorgchem.8b00365>

- [27] Zhang C, Wang X, Liang Q et al (2016) Amorphous phosphorus/Nitrogen-doped graphene paper for ultra-stable Sodium-ion batteries. *Nano Lett* 16:2054–2060. <https://doi.org/10.1021/acs.nanolett.6b00057>
- [28] Li W, Hu S, Luo X et al (2017) Confined amorphous red phosphorus in MOF-derived N-doped microporous carbon as a superior anode for sodium-ion battery. *Adv Mater* 29(16):1605820. <https://doi.org/10.1002/adma.201605820>
- [29] Han Y, Qi P, Li S et al (2014) A novel anode material derived from organic-coated ZIF-8 nanocomposites with high performance in lithium ion batteries. *Chem Commun* 50:8057–8060. <https://doi.org/10.1039/c4cc02691h>
- [30] Wang J, Wang G, Wang H (2015) Flexible free-standing Fe<sub>2</sub>O<sub>3</sub>/graphene/carbon nanotubes hybrid films as anode materials for high performance lithium-ion batteries. *Electrochim Acta* 182:192–201. <https://doi.org/10.1016/j.electacta.2015.09.080>
- [31] Yang D, Xu S, Dong S et al (2015) Facile synthesis of free-standing Fe<sub>2</sub>O<sub>3</sub>/carbon nanotube composite films as high-performance anodes for lithium-ion batteries. *RSC Adv* 5:106298–106306. <https://doi.org/10.1039/c5ra21609e>
- [32] Wang H, Yuan S, Ma D, Zhang X, Yan J (2015) Electrospun materials for lithium and sodium rechargeable batteries: from structure evolution to electrochemical performance. *Energy Environ Sci* 8:1660–1681. <https://doi.org/10.1039/c4ee03912b>
- [33] Niederberger M (2007) Nonaqueous sol–gel routes to metal oxide nanoparticles. *Acc Chem Res* 40:793–800. <https://doi.org/10.1021/ar600035e>
- [34] Gan Y, Xu F, Luo J et al (2016) One-pot biotemplate synthesis of FeS<sub>2</sub> decorated Sulfur-doped carbon fiber as high capacity anode for lithium-ion batteries. *Electrochim Acta* 209:201–209. <https://doi.org/10.1016/j.electacta.2016.05.076>
- [35] Huang P, Tao W, Wu H et al (2017) N-doped coaxial CNTs@ $\alpha$ -Fe<sub>2</sub>O<sub>3</sub>@C nanofibers as anode material for high performance lithium ion battery. *J Energy Chem* 27(5):1453–1460. <https://doi.org/10.1016/j.jechem.2017.09.011>
- [36] D Yang, L K, M Zhong, J Zhu, and X Bu (2018) Metal–organic gel-derived Fe<sub>x</sub>O<sub>y</sub>/nitrogen-doped carbon films for enhanced lithium storage. *Small* 1804058. <https://doi.org/10.1002/smll.201804058>
- [37] Zhou G, Wang D, Yin L, Li N, Li F, Cheng H (2012) Oxygen bridges between NiO nanosheets and graphene for improvement of Lithium storage. *ACS Nano* 6:3214–3223
- [38] Dresselhaus MS, Jorio A, Hofmann M, Dresselhaus G, Saito R (2010) Perspectives on carbon nanotubes and graphene raman spectroscopy. *Nano Lett* 10:751–758. <https://doi.org/10.1021/nl904286r>
- [39] Zhou J, Song H, Ma L, Chen X (2011) Magnetite/graphene nanosheet composites: interfacial interaction and its impact on the durable high-rate performance in lithium-ion batteries. *RSC Adv* 1:782–791. <https://doi.org/10.1039/c1ra00402f>
- [40] Li Z, Tang B (2017) Mn<sub>3</sub>O<sub>4</sub>/nitrogen-doped porous carbon fiber hybrids involving multiple covalent interactions and open voids as flexible anodes for lithium-ion batteries. *Green Chem* 19:5862–5873. <https://doi.org/10.1039/c7gc02786a>
- [41] Ma J, He Y, Zhang W et al (2015) An experimental insight into the advantages of in situ solvothermal route to construct 3D graphene-based anode materials for lithium-ion batteries. *Nano Energy* 16:235–246. <https://doi.org/10.1016/j.nanoen.2015.06.026>
- [42] Delamar M, Combellas Catherine, Kanoufi Fre ´ric, Pinson Jean, Podvorica ´de Fetah I (2005) Spontaneous grafting of iron surfaces by reduction of aryldiazonium salts in acidic or neutral aqueous solution. *Chem Mater* 17:3968–3975
- [43] Nguyen T, Lee S (2017) Green synthesis of N-doped carbon modified iron oxides (N-Fe<sub>2</sub>O<sub>3</sub>@Carbon) using sustainable gelatin cross-linker for high performance Li-ion batteries. *Electrochim Acta* 248:37–45. <https://doi.org/10.1016/j.electacta.2017.07.114>
- [44] Guo H, Li T, Chen W et al (2014) General design of hollow porous CoFe<sub>2</sub>O<sub>4</sub> nanocubes from metal–organic frameworks with extraordinary lithium storage. *Nanoscale* 6:15168–15174. <https://doi.org/10.1039/c4nr04422c>
- [45] Wu H, Chen J, Hng H, Lou X (2012) Nanostructured metal oxide-based materials as advanced anodes for lithium-ion batteries. *Nanoscale* 4:2526–2542. <https://doi.org/10.1039/c2nr11966h>
- [46] Guo W, Sun W, Lv L, Kong S, Wang Y (2017) Microwave-assisted morphology evolution of Fe-based metal-organic frameworks and their derived Fe<sub>2</sub>O<sub>3</sub> nanostructures for li-ion storage. *ACS Nano* 11:4198–4205. <https://doi.org/10.1021/acsnano.7b01152>
- [47] Gao G, Zhang Q, Wang K, Song H, Qiu P, Cui D (2013) Axial compressive  $\alpha$ -Fe<sub>2</sub>O<sub>3</sub> microdisks prepared from CSS template for potential anode materials of lithium ion batteries. *Nano Energy* 2:1010–1018. <https://doi.org/10.1016/j.nanoen.2013.03.023>
- [48] Sun C, Chen S, Li Z (2018) Controllable synthesis of Fe<sub>2</sub>O<sub>3</sub>-carbon fiber composites via a facile sol–gel route as anode materials for lithium ion batteries. *Appl Surf Sci* 427:476–484. <https://doi.org/10.1016/j.apsusc.2017.08.070>
- [49] Jia X, Chen J, Xu J et al (2012) Fe<sub>2</sub>O<sub>3</sub> xerogel used as the anode material for lithium ion batteries with excellent electrochemical performance. *Chem Comm* 48:7410–7412. <https://doi.org/10.1039/c2cc33469k>
- [50] Son M, Hong Y, Lee J, Kang Y (2013) One-pot synthesis of Fe<sub>2</sub>O<sub>3</sub> yolk-shell particles with two, three, and four shells for

- application as an anode material in lithium-ion batteries. *Nanoscale* 5:11592–11597. <https://doi.org/10.1039/c3nr03978a>
- [51] Ko Y, Park S, Jung K, Kang Y (2013) One-pot facile synthesis of ant-cave-structured metal oxide-carbon microballs by continuous process for use as anode materials in Li-ion batteries. *Nano Lett* 13:5462–5466. <https://doi.org/10.1021/nl4030352>
- [52] Li W, Li Z, Yang F, Fang X, Tang B (2017) Synthesis and electrochemical performance of SnO<sub>x</sub> quantum dots@UiO-66 hybrid for lithium ion battery applications. *ACS Appl Mater Interfaces* 9:35030–35039. <https://doi.org/10.1021/aciamsi.7b11620>